Progress In Electromagnetics Research C, Vol. 137, 1–16, 2023

Systematic Performance Evaluation for the Detection of Breast Tumors with Sinusoidal Corrugated Antipodal Vivaldi Antennas Utilizing DAS and It-DAS Methodologies

Athul O. Asok, Ayush Tripathi, and Sukomal Dey*

Abstract—This work presents a study where a Sinusoidal Corrugated Antipodal Vivaldi Antenna (SC-AVA) operating in the Ultra-Wideband (UWB) region is employed as a transducer for microwave imaging of a cancerous breast. The functionality of the antenna within the UWB range is initially confirmed through thorough testing of performance parameters, including return loss, gain, radiation pattern, and group delay. Subsequently, its practical application in biomedical imaging is evaluated by measuring Specific Absorption Rate (SAR) readings at multiple frequencies within the operational range. The SAR readings are obtained from an EM simulator by modelling both homogeneous and heterogeneous breast phantoms and placing them in close proximity to the transducer. The SAR values are recorded at various frequencies, and it is determined that these readings comply with the Federal Communication Commission (FCC) regulations. The modelled SC-AVA is further utilized in the detection of a single tumor in a homogeneous breast phantom and multiple tumors in a realistic heterogeneous breast phantom. These phantoms are developed in a laboratory environment and imaged using an in-house developed monostatic microwave imaging setup. To gather preliminary information about the target, a homogeneous phantom with one tumor is imaged initially. Subsequently the heterogeneous phantom with two embedded tumors is imaged in this study. The imaging results demonstrate that tumors of different sizes can be clearly visualized in both breast phantoms using the SC-AVA, employing image reconstruction algorithms such as Delay and Sum (DAS) and iterative Delay and Sum (it-DAS). Furthermore, a comparison of the reconstructed images reveals that the it-DAS reconstruction algorithm produces images with improved clarity compared to the DAS algorithm.

1. INTRODUCTION

According to available data, it has been determined that more than 1.8 million new cases of adenocarcinoma are diagnosed annually. The achievement of a high survival rate of 97% in breast cancer therapy depends on its early identification [1]. Therefore, there is a critical need for an on-site rapid and portable diagnostic device to ensure the prompt detection of breast cancer [2]. Several recognized methods exist for the detection of breast cancer. The primary method involves clinical breast examination, followed by techniques such as X-ray mammography, Ultrasonography (US), Magnetic Resonance Imaging (MRI), and Positron Emission Tomography (PET). X-ray mammography is the most commonly used method for detecting cancerous growths in various parts of the human body. However, this method utilizes highly ionizing X-rays to image internal body parts, which can be harmful, and its repeated exposure may even induce cancer in individuals undergoing mammography. Additionally, the breast compression involved in the procedure can cause the patient discomfort. On the other hand, MRI utilizes radio waves to generate images of the target without causing harm to the human body. MRI

Received 27 June 2023, Accepted 9 August 2023, Scheduled 23 August 2023
* Corresponding author: Sukomal Dey (sukomal.iitpkd@gmail.com).
The authors are with the Department of Electrical Engineering, Indian Institute of Technology Palakkad, India.

scans also provide excellent visualization of hidden tumors within the body. Nevertheless, MRI scans are expensive, and obtaining test results takes longer time than other procedures. As a result, MRI devices cannot be repeatedly used for imaging the human breast. PET scans involve the injection of a radioactive tracer directly into the body to identify regions with tumors by tracking the absorption of the tracer by the body tissues. However, apart from the time required to complete the tumor identification process, the primary concern is the injection of an external substance into the human body. These limitations in existing technologies have served as motivation to develop a novel imaging technique that overcomes the constraints imposed by current methods.

Microwave Imaging (MI), which employs electromagnetic radiation, is a non-destructive technique used to detect the presence, size, and location of various objects. Microwave imaging has extensive applications, including the diagnosis of adenocarcinoma, detection of brain stroke, identification of corrosion in metal rods used for construction, and detection of oil well leakages, among others. Microwave imaging uses non-ionizing radiation to scan the target without causing any harm. These technologies are also more cost-effective compared to other globally used imaging systems. Moreover, once the entire system is operational, qualified personnel are not required to operate a microwave imaging system. These advantages highlight the benefits of microwave imaging over the widely popular techniques.

The design of antennas plays a vital role in microwave imaging as it significantly impacts the sharpness of the reconstructed image. Various antenna designs, including pyramidal horn antennas [3], Vivaldi antennas [4–6], Coplanar Waveguide (CPW) antennas [7], and Electromagnetic Band Gap (EBG) antennas [8], have been recommended for breast phantom measurements. For an efficient microwave imaging system, the transducer must possess broadband capabilities, be compact, directional, and have high radiation efficiency. Therefore, in the proposed work, an AVA that meets all these requirements is utilized to image various breast phantoms. In imaging applications, UWB antennas are essential as the low-frequency range controls the depth of penetration, while the high-frequency range ensures the resolution of the reconstructed image. Different types of Vivaldi antennas and their antipodal counterparts are discussed in [10–14]. This manuscript presents a Sinusoidal Corrugated Antipodal Vivaldi Antenna (SC-AVA) operating in the UWB range. The manuscript comprehensively analyzes the performance of the antenna in both the time and frequency domains. Furthermore, the imaging capability of the antenna is examined to an acceptable extent using breast phantoms developed with widely recognized image reconstruction algorithms such as Delay and Sum (DAS) algorithm and iterative Delay and Sum (it-DAS).

The entire paper is organized as follows. Section 2 provides an in-depth explanation of the modeling and analysis of the UWB SC-AVA, discussing both the time domain and frequency domain analyses. Section 3 details the design of the breast phantoms and validates them through Specific Absorption Rate (SAR) measurements. Also, the E-field and H-field analyses are done in the same section. Section 4 elaborates the fabrication procedure of the breast phantoms and presents the image reconstruction using DAS and it-DAS techniques. Finally, the conclusion, summarizing the complete work, is discussed in Section 5.

2. THE ANTENNA GEOMETRY DESIGN AND ANALYSIS

The complete design methodologies of the proposed antenna are given in [14]. The antenna design is optimized in full wave simulation [14], and the fabricated device is displayed in Fig. 1. The SC-AVA is measured in an anechoic chamber environment, and the return loss results are compared with its simulated counterparts, displayed in Fig. 2(a). It is found that the measured and simulated responses are in close agreement to each other. Also, the circuit simulation response is displayed in the same figure along with its simulated and measured counterparts for better clarity. It is also observed that the circuit simulation plots are also in agreement with the other two plots. The gain of the designed SC-AVA is measured and compared with the simulated responses. It is observed that the simulated and measured responses are in agreement with minor mismatches, as shown in Fig. 2(b). Measured versus simulated E-plane and H-plane radiation patterns are depicted in Fig. 3 and Fig. 4, respectively, at 8 GHz and 10 GHz. The measured performance indicates the usefulness of the proposed antenna for imaging application.

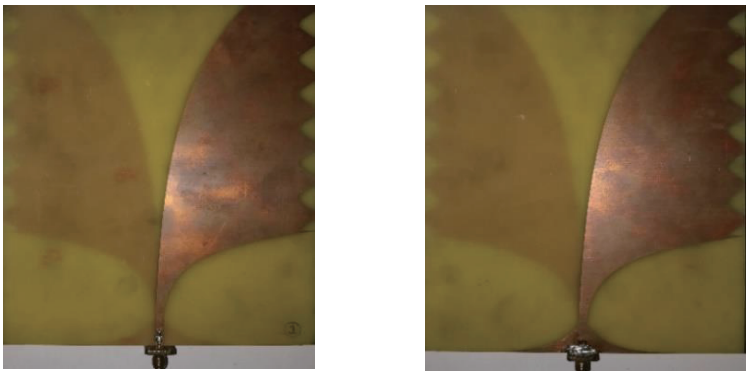

(a) (b)

Figure 1. The fabricated SC-AVA. (a) Front side and (b) Back side.

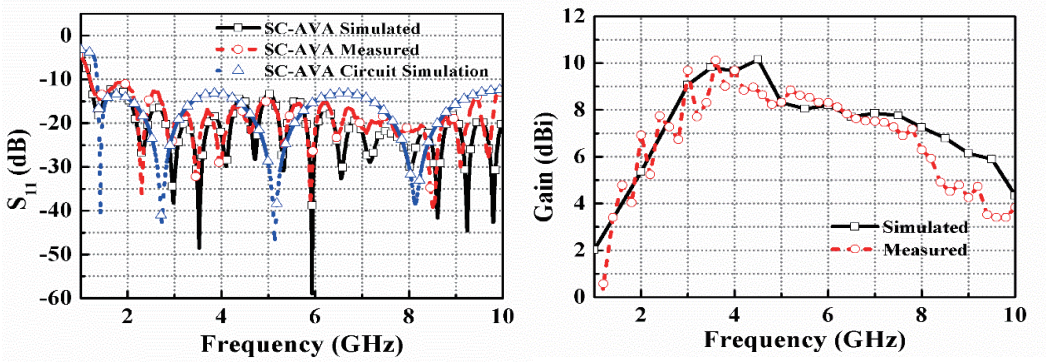

(a) (b)

Figure 2. The comparison of the simulated antenna response with its measured counterpart. (a) Return loss and (b) gain response.

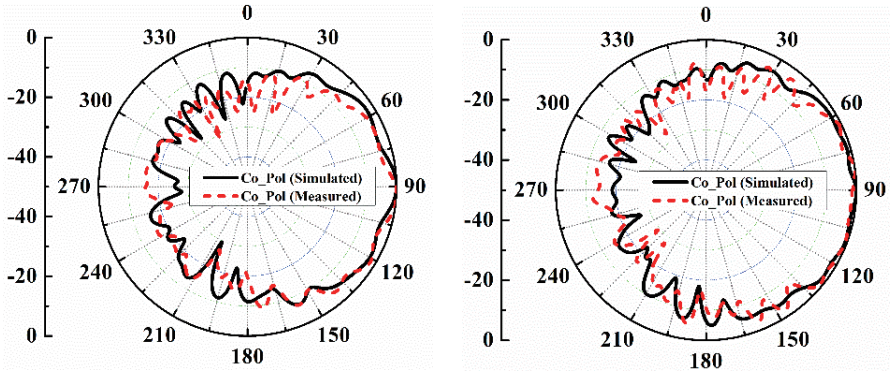

(a) (b)

Figure 3. The *E*-plane radiation pattern of the designed device at (a) 8 GHz and (b) 10 GHz.

In order to assess the suitability of the proposed antenna for employment in the MI technique, a comprehensive analysis of its time-domain characteristics is essential. This analysis encompasses the examination of various factors, such as the transmitted-received signal, fidelity factor, and group delay. To evaluate the signal shaping properties and potential signal distortion of the antenna, three distinct configurations were investigated. These configurations involved two front to front arrangements and one side by side arrangement, with a 200 mm gap maintained between the transmitter and receiver

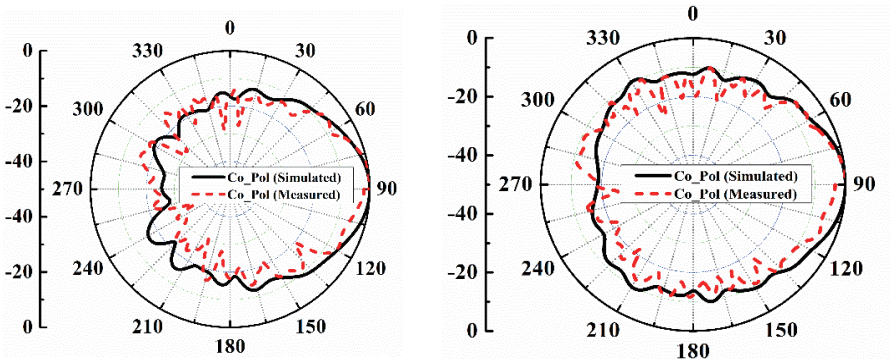

Figure 4. The H-plane radiation pattern of the designed device at (a) 8 GHz and (b) 10 GHz.

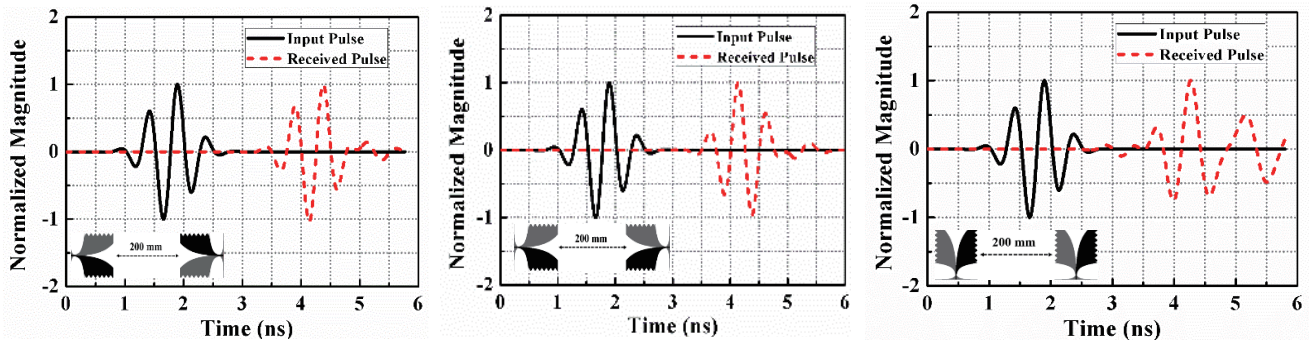

Figure 5. Normalized magnitude of transmitted signal and received signal for (a) front to front with antipodal sections opposite to each other, (b) front to front with antipodal sections on the same side and (c) side by side configuration.

antennas. The normalized magnitude with respect to time is displayed in Figs. 5(a)–(c). The same figure also presents the various antenna arrangements for assessing the reliability of the antenna for imaging applications. Various combinations like front to front with antipodal sections opposite to each other (Fig. 5(a)), front to front with antipodal sections on the same side (Fig. 5(b)), and side by side (Fig. 5(c)) configurations are considered. In the case of face-to-face configurations (Figs. 5(a) and (b)), it is evident that the received signals closely resemble the emitted signals as compared to the side by side configuration, indicating strong guided radiation. Therefore, for breast imaging applications using microwave technology, the face to face setup is recommended. The calculation of the cross-correlation between the transmitted and received signals is performed using Equation (1), commonly referred to as the Fidelity Factor (FF) [15]. This factor serves as a measure of the similarity between the transmitted and received signals.

$$FF = \max_{\tau} \left| \frac{\int_{-\infty}^{+\infty} S(t)\, r(t-\tau) dt}{\int_{-\infty}^{+\infty} S(t)^2 \cdot \int_{-\infty}^{+\infty} r(t)^2 dt} \right| \tag{1}$$

where $s(t)$ and $r(t)$ represent transmitted and received signals, respectively, and τ represents the group delay. The FF values for different configurations of the antenna are as follows: for the front-to-front configuration with antipodal sections on the opposite side, the FF value is 98.4%; for the front-to-front configuration with antipodal sections on the same side, the FF value is 90.6%; and for the side-by-side

configuration, the FF value is 70.7%. The high FF value observed in the front-to-front configuration indicates that the transmitted signal experiences less distortion in this arrangement.

Another crucial aspect in evaluating the performance of the antenna in time domain is the group delay, which characterizes the phase distortion of the signal. The group delay is defined as the negative derivative of the transfer function phase, $\varphi(\omega)$, with respect to frequency [15]. It provides an estimate of the time required for a signal to pass through the antenna. The group delay can be computed using Equation (2) as,

$$\tau(\omega) = -\frac{d\varphi(\omega)}{d\omega} = -\frac{d\varphi(\omega)}{2\pi df} \tag{2}$$

A flat response is critical for UWB applications. Fig. 6. illustrates the estimated group delay for the proposed work using the three different combinations. The variations in group-delay remains within an acceptable range of up to 3.8 ns for both the front to front configurations and is distorted in the case of side by side configuration. Considering both the FF and group delay, the front to front setup is recommended for MI.

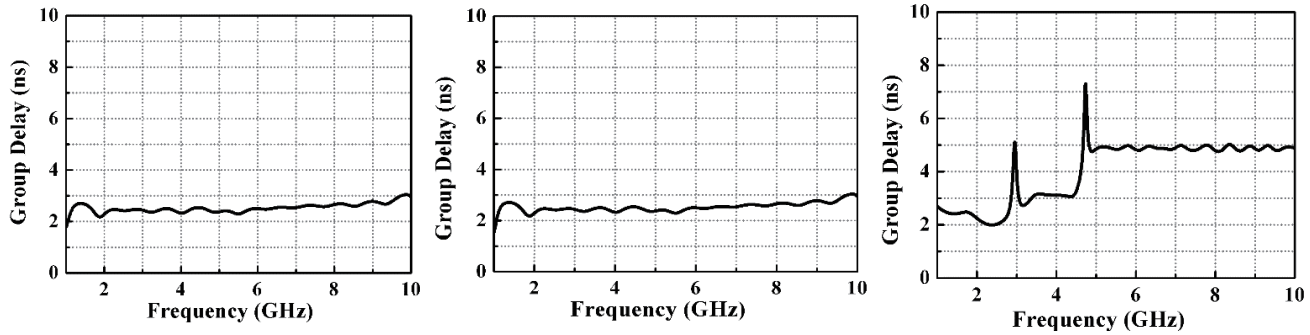

Figure 6. The simulated group delay for (a) front to front with antipodal sections opposite to each other, (b) front to front with antipodal sections on the same side and (c) side by side configuration.

3. BREAST PHANTOM DESIGN AND PERFORMANCE ANALYSIS IN THE SIMULATOR

3.1. Breast Phantom Design in the Simulator

Two breast phantoms were simulated using the CST simulator: a homogeneous breast phantom and a heterogeneous breast phantom. The homogeneous breast phantom consisted of a fat layer with a radius of 60 mm (R_1), and a single tumor with a radius of 4 mm (R_2) was embedded at its center. This phantom served as a preliminary analysis before investigating more complex breast models. The heterogeneous breast phantom comprised three layers: a skin layer with a radius of 60 mm (R_3), a fat layer with a radius of 58 mm (R_4), and a gland layer with a radius of 50 mm (R_5). Within the gland layer, two tumors were inserted, each with a radius of 5 mm (R_6, R_7). The materials available in the CST simulator library

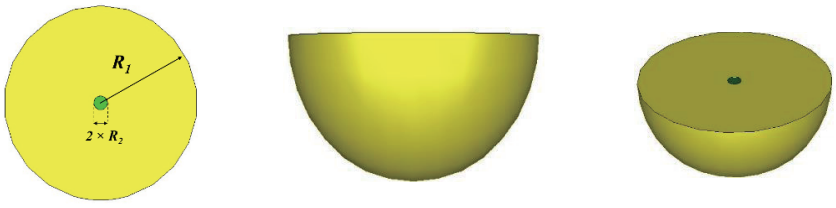

Figure 7. The modelled homogeneous breast phantom in the simulator with one embedded tumor. (a) Top view. (b) Front view and (c) perspective view.

were employed to accurately model the phantoms. Fig. 7 illustrates the modeled homogeneous breast phantom with a single tumor, presenting various orientations within the same figure. Furthermore, Fig. 8 showcases the modeled heterogeneous breast phantom with two tumors, along with different orientations, providing a comprehensive visualization of the phantom configurations and arrangements.

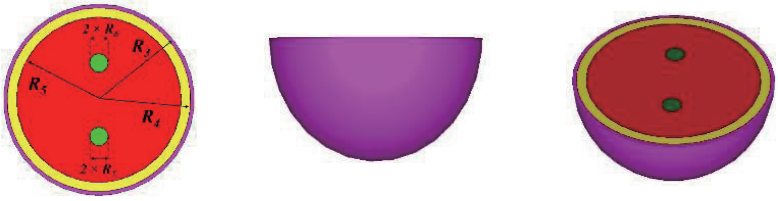

Figure 8. The modelled heterogeneous breast phantom in the simulator with two embedded tumors. (a) Top view. (b) Front view and (c) perspective view.

3.2. Monostatic SAR Analysis in the Simulator

The simulator is also utilized to conduct an SAR analysis of the proposed antenna. SAR, which stands for Specific Absorption Rate, quantifies the level of Radio Frequency (RF) power absorbed by the human body. It is expressed according to (3) as,

$$\mathrm{SAR} = \frac{\sigma \left|E\right|^2}{\rho} \tag{3}$$

where σ is the conductivity (S/m) of the tissue, E the internal electric field intensity (V/m), and ρ the mass density (kg/m^3). The SAR value is calculated only for the heterogeneous breast phantom with two embedded tumors as the heterogeneous breast phantom represents a model close to the actual cancerous breast. The SAR analysis setup in the simulator for homogeneous and heterogeneous breast phantoms is displayed in Fig. 9. The SAR values obtained at 4 GHz, 6 GHz, 8 GHz, and 10 GHz when being averaged over 1 g of tissue are displayed in Fig. 10. The obtained SAR readings are further tabulated in a Table 1 for clarity. It is observed that the SAR readings comply with Federal Communication Commission (FCC) guidelines.

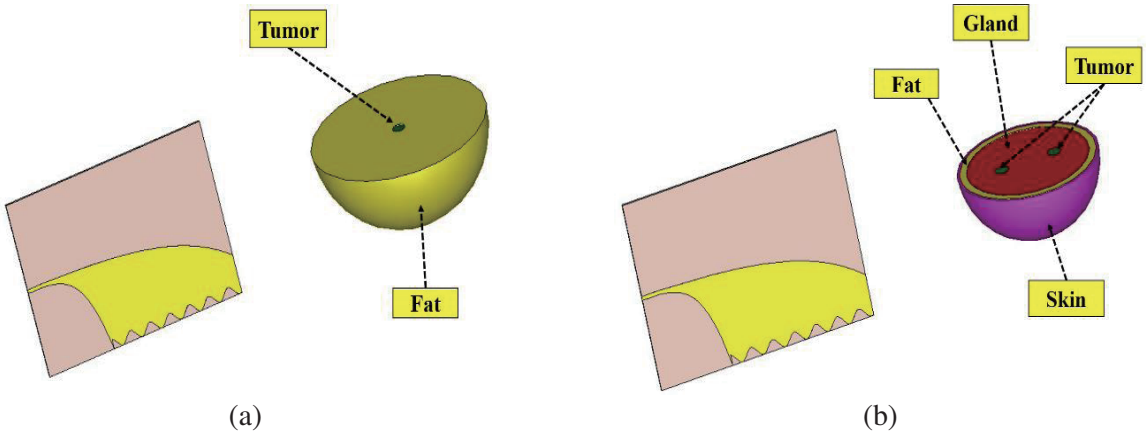

Figure 9. The SAR analysis setup in the simulator. (a) Homogeneous case and (b) Heterogeneous case.

3.3. E-Field and H-Field Analysis with a Single Antenna

In order to evaluate the performance of the antenna for MI, a comprehensive analysis was conducted to assess the penetration of both the electric field (E-field) and magnetic field (H-field) from various

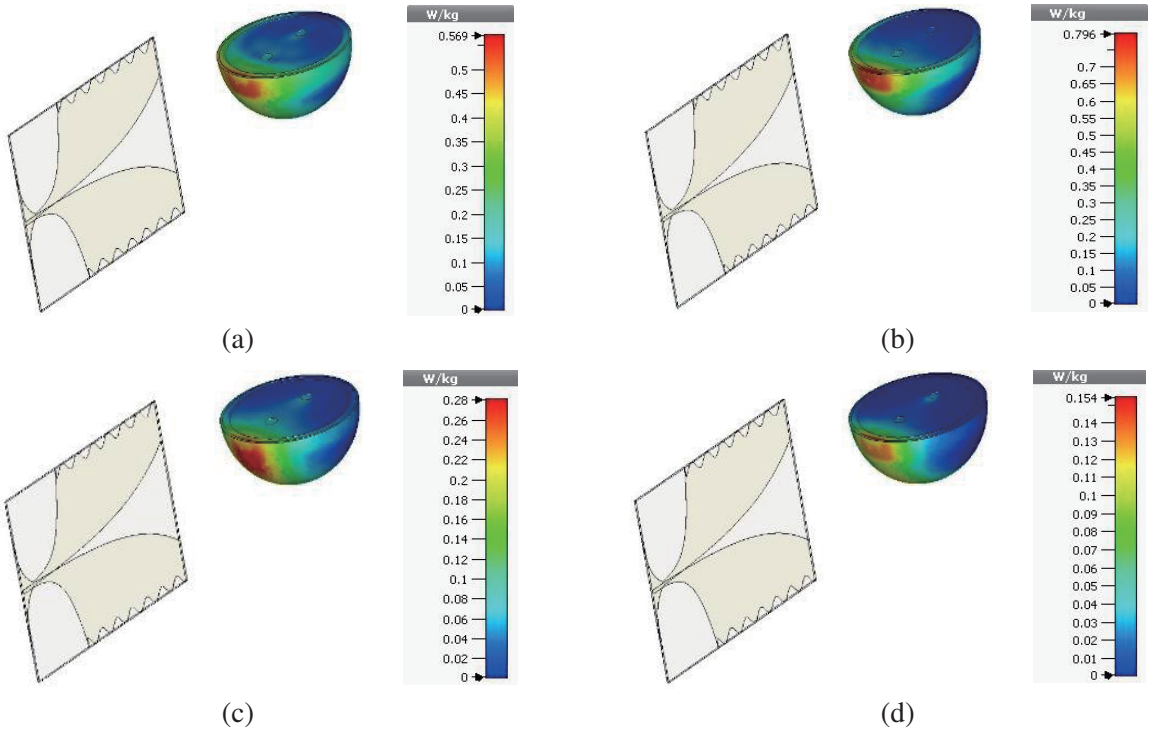

Figure 10. Heterogeneous breast phantom SAR readings when averaged over 1g of tissue at (a) 4 GHz, (b) 6 GHz, (c) 8 GHz and (d) 10 GHz.

Table 1. Heterogeneous breast phantom SAR values.

Frequency (GHz)	SAR (1 g) (W/Kg)
4 GHz	0.569
6 GHz	0.796
8 GHz	0.28
10 GHz	0.154

perspectives. Figs. 11(a)–(d) depict the infiltration of the E-field in the YZ-plane within the heterogeneous breast model at frequencies of 4 GHz, 6 GHz, 8 GHz, and 10 GHz, respectively. The illustrations clearly indicate that the E-field effectively penetrates the breast tissue, reaching a significant depth. Similarly, the penetration of the H-field in the YZ-plane within the same breast model is showcased in Figs. 12(a)–(d). These figures demonstrate the propagation of the H-field and its penetration within the breast tissue at the aforementioned frequencies. Due to the lossy nature of the breast tissues, the intensity of the H-field decreases as it spreads. However, the antenna exhibits nearly directional propagation characteristics, leading to enhanced infiltration of the electromagnetic fields within the breast tissues. By analyzing the E-field and H-field penetration from different perspectives, it becomes evident that the antenna can effectively penetrate the breast tissue, allowing for the capture of valuable information. Additionally, the evaluation of signal penetration depth within the breast tissues ensures that the antenna can gather relevant data to reconstruct a usable and accurate breast image. The ability to detect and analyze dispersion signals within the breast tissue is crucial for obtaining informative images.

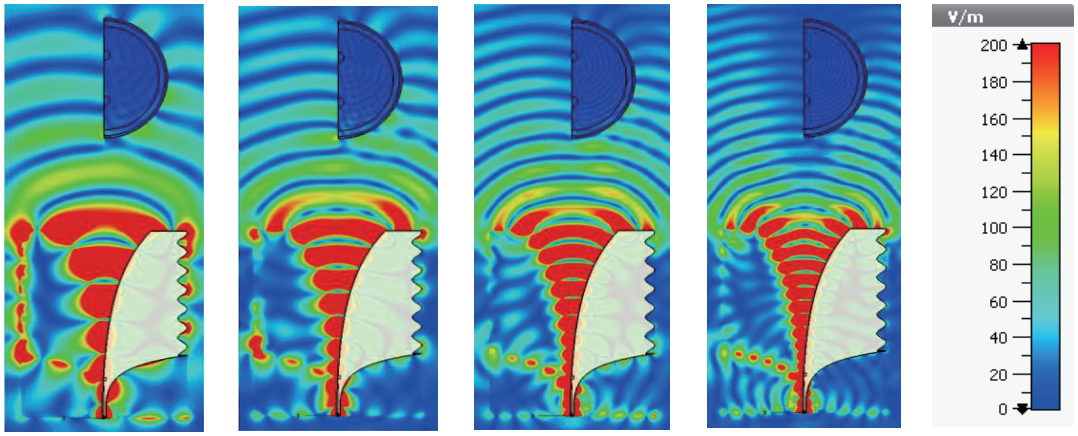

Figure 11. The simulated E-field distribution of the antenna with heterogeneous breast phantom at (a) 4 GHz, (b) 6 GHz, (c) 8 GHz and (d) 10 GHz. (e) displays the scaling.

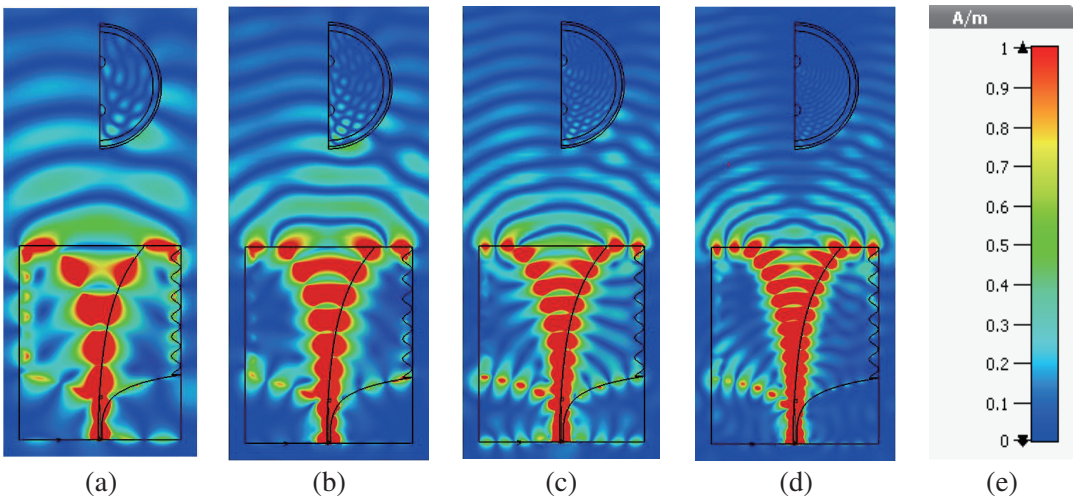

Figure 12. The simulated H-field distribution of the antenna with heterogeneous breast phantom at (a) 4 GHz, (b) 6 GHz, (c) 8 GHz and (d) 10 GHz. (e) displays the scaling.

4. BREAST PHANTOM FABRICATION AND IMAGING

4.1. Homogeneous and Heterogeneous Breast Phantom Fabrication

The fabrication process for homogeneous phantoms follows the method described in [16]. The fat layer is prepared by dissolving agar-agar in water, adding sodium chloride, sodium dehydroacetate monohydrate, xanthan gum, and polyethylene powder. Yellow food color is added for distinction. The mixture is poured into a stainless-steel mold resembling a real breast shape. Tumor material is prepared using a similar procedure with different quantities and blue color for differentiation. The tumor is inserted into the fat layer, and the phantom is refrigerated. Fig. 13(a) shows the homogeneous phantom with a single tumor.

For the heterogeneous phantom, propylene glycol is mixed with water and heated. Agar-agar, gelatin powder, surfactant, formalin, and safflower oil are added. The mixture is cooled, poured into a mold, and layered as skin, fat, and gland based on the different ratios of the materials described above. Holes are made in the gland layer, and the tumor mixture is poured in. The different layers are

(a) (b)

Figure 13. The fabricated breast phantoms. (a) Homogeneous breast phantom with single tumor and (b) heterogeneous breast phantom with two tumors.

differentiated with food colors, and the phantom is refrigerated. Fig. 13(b) displays the heterogeneous breast phantom with two tumors inserted.

4.2. Image Reconstruction Procedure

The complete imaging setup is displayed in Fig. 14. Please note that the monostatic approach is used for image reconstruction. In the starting stage, the homogeneous phantom is placed on the turntable of the imaging setup. Then, the placed phantom is rotated in 40-degree step size to obtain a total of 9 sets of readings from the Performance Network Analyzer (PNA), which are serially stored in the computer connected to it. This step is followed by replacing the first breast phantom with the next one, and the same steps are repeated. The frequency domain data corresponding to each antenna rotation is extracted from the Vector Network Analyzer (VNA). The DAS technique is used to image the phantom first followed by the it-DAS method.

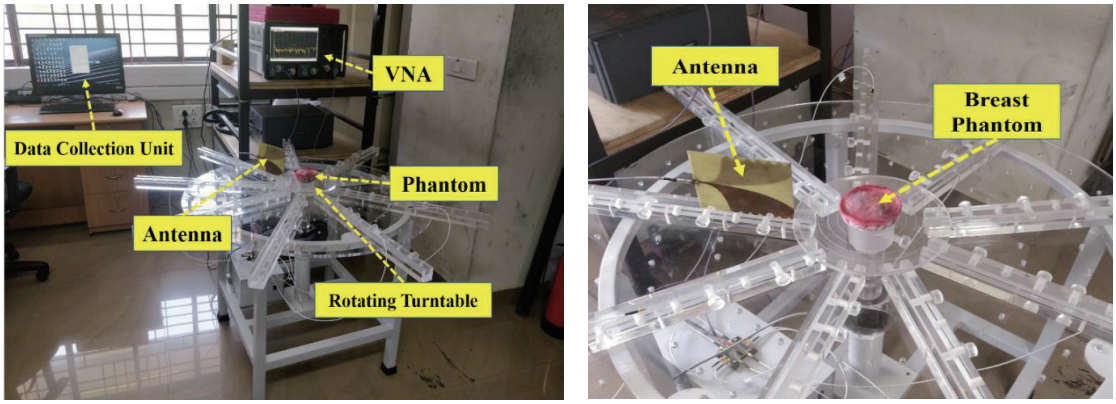

(a) (b)

Figure 14. The complete imaging setup. (a) The in-house developed imaging setup and (b) the magnified view of the turntable used for imaging.

The DAS is the preliminary technique used to obtain the image of the tumors in the utilized phantom. During DAS, an artificial focus point is made by summing up the time shifted signals obtained after the frequency to time conversion of the reflected signals obtained from the PNA. The summed up point will have a higher intensity than the remaining points in the image space. The image space is observed by plotting the intensity vs the position in Python environment to display the images. The DAS algorithm is expressed as (4),

$$Y_{DAS} = \sum_{I=1}^{M} |b_i(t-\tau)| \tag{4}$$

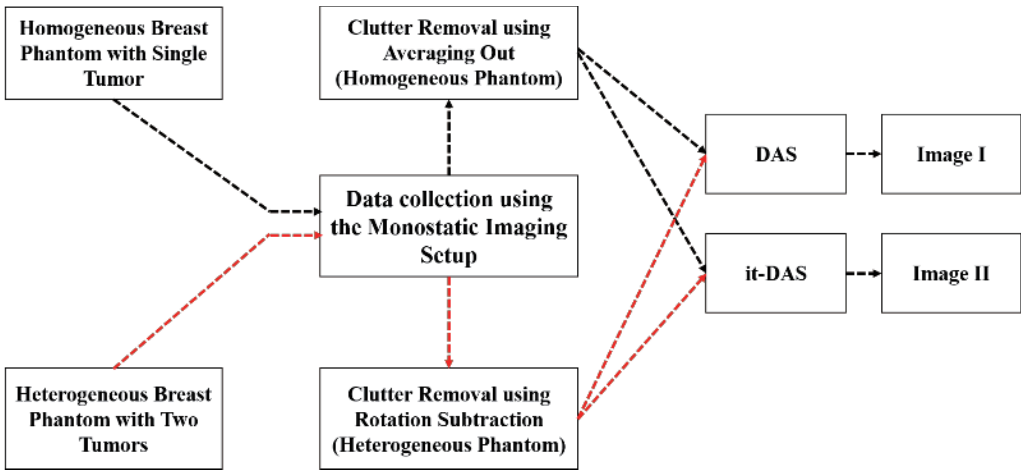

Figure 15. The flow chart of the image reconstruction process.

where Y_{DAS} is the DAS signal, and $bi(t-\tau)$ is the delay compensated signal. After the image reconstruction using DAS method, the it-DAS algorithm is used to reconstruct the same target. The it-DAS process adopts the iterative form of the Maximum Likelihood Expectation Maximization (MLEM) algorithm utilized in PET [17]. This algorithm has a functional form that references only the forward and back projections of the imaging system. This functional form is displayed in Equation (5) with an additional normalization factor $\hat{F}[U]$ multiplying the dataset D,

$$I^{n+1} = \frac{I^n}{\hat{B}[U]}\hat{B}\left[\frac{D \cdot \hat{F}[U]}{\hat{F}[I^n]}\right] \tag{5}$$

where $\hat{B}$ denotes the back projection operator, $\hat{F}$ the forward projection operator, D the set of the experimentally measured data, U a unity matrix, and I^n the image estimate at the nth iteration. $\hat{B}$ transforms data from the time domain to the spatial domain, and $\hat{F}$ simulates the dataset that would be obtained if the system scanned an object that would reproduce the image estimate. The iterative structure as displayed in (5) was adopted for the use in breast microwave radar imaging using the DAS algorithm as the back-projection operator. This gives the it-DAS algorithm. Also, please note that two separate clutter removal algorithms are used for both the homogenous and heterogeneous cases. The averaging method discussed in [18] is utilized in homogeneous case, and the rotation subtraction method elaborated in [19] is utilized for heterogeneous breast phantom imaging. A generalized flowchart of the image reconstruction process is shown depicted in Fig. 15.

The reconstructed images of the homogeneous breast phantom with single tumor using DAS and it-DAS algorithms are displayed in Figs. 16(a) and (b). The reconstructed images of the heterogeneous breast using DAS and it-DAS algorithms are displayed in Figs. 17(a) and (b). The embedded tumors are appropriately identified up to a reasonable extent. Also it can be observed that the it-DAS algorithm obtains the image with reduced false positive intensities. Minor deviations from the exact tumor locations are also observed in all the cases. This can be attributed to the measurement errors while taking the readings with the phantoms, irregularity while placing the phantom in the turntable, losses from the RF switch, cable losses, and the reflections from the nearby surfaces.

The work done is compared to some of the recent works [20–37] in literature which is listed in Table 2. It can be observed that in the proposed work, the single tumor in the homogeneous breast phantom and two tumors in the heterogeneous breast phantom are detected clearly. The antenna also attains a higher gain than some of the other works in literature. The proposed work reconstructs compact tumors as compared to some of the recent works in literature. A few more works related to UWB antennas and their imaging applications can be found in [38–56].

Table 2. Comparison the imaging results with similar breast imaging works.

Ref	Antenna Used	BW (GHz)	Max. Gain (dBi)	FBW%	Phantom Used	Imaging Method	No of IA used	Tumor Number	Min. TR (mm)	Phantom Complexity
[20]	Side slotted Vivaldi antenna	2.8 –7	~8	85.71	Heterogeneous	DAS, IC-DAS	1	2	5	High
[21]	Balanced slotted antipodal Vivaldi Antenna	3.01 - 11	7.1	114.06	Homogeneous	DMAS	1	1	5	Less
[22]	Unidirectional UWB Antenna	UWB	NG	109.48	Not Given	DMAS	1	NG	NG	NM
[23]	AMC Inspired CPW Fed Patch Antenna	3 - 8	~10	90.90	Commercial	DMAS	1	1	5	High
[24]	Flexible Monopole Antenna	NG	NG	NG	Human	DMAS	1	NG	NG	High
[25]	Multilayered metamaterials array antenna	4.1 – 9.7	5.7	81.15	Simulated	NG	NG	1	5	Less
[26]	Microstrip Patch Antenna	3 - 9	4.5	100	NG	SAR	1	1	NG	Less
[27]	Sierpinski fractal DRA	5.6 – 14.2	5.8	86.86	Homogeneous	CF-DAS, CF-DMAS	2	1	5	Less
[28]	Metamaterial-Loaded Log Periodic Antenna	2 - 5	5.5	85.71	Homogeneous	DAS, DMAS	2	1, 2	5	Less
[29]	CPW-Fed Flexible UWB Antenna	2.26 – 13.71	3.84	143.39	Homogeneous	NG	NG	1	4	Less
[30]	Vivaldi Antenna	2.5 – 8.5	8.5	109.09	Homogeneous	NG	NG	NG	NG	Less
[31]	Vivaldi Antenna	0.5 – 4.5	7	160	NG	NG	NG	NG	NG	NG
[32]	Vivaldi Antenna	1.54 - 7	8.5	127.86	Homogeneous	NG	1	1	NG	Less
[33]	Vivaldi Antenna	2.5 - 11	7.2	125.92	Homogeneous (Simulated)	NG	1	1	NG	Less
[34]	NG	NG	NG	NG	Homogeneous	NG	1	1	NG	Less
[35]	NG	NG	NG	NG	Human	NG	NG	NG	NG	High
[36]	Planar UWB Antenna Array	3.5 - 15	NG	124.32	Heterogeneous	CMI	1	1,2	NG	High
[37]	Slotted UWB Antenna	3.5 - 12	8	109.8	Homogeneous (Simulated)	NG	1	1	NG	Less
This Work	**SC-AVA**	**1.1 - 10**	**10**	**163.63**	**Heterogeneous**	**DMAS, it-DMAS**	**2**	**4**	**4**	**High**

NG - Not Given, BW – Bandwidth, FBW – Fractional Bandwidth, IA- Imaging Algorithms, TR-Tumor Radius, UWB – Ultra-Wideband, AMC-Artificial Magnetic Conductor, CPW-Coplanar Waveguide, DRA-Dielectric Resonator Antenna, IC- Iteratively corrected, CF- Coherence Factor, SAR-Synthetic Aperture, Radar, CMI-Confocal Microwave Imaging.

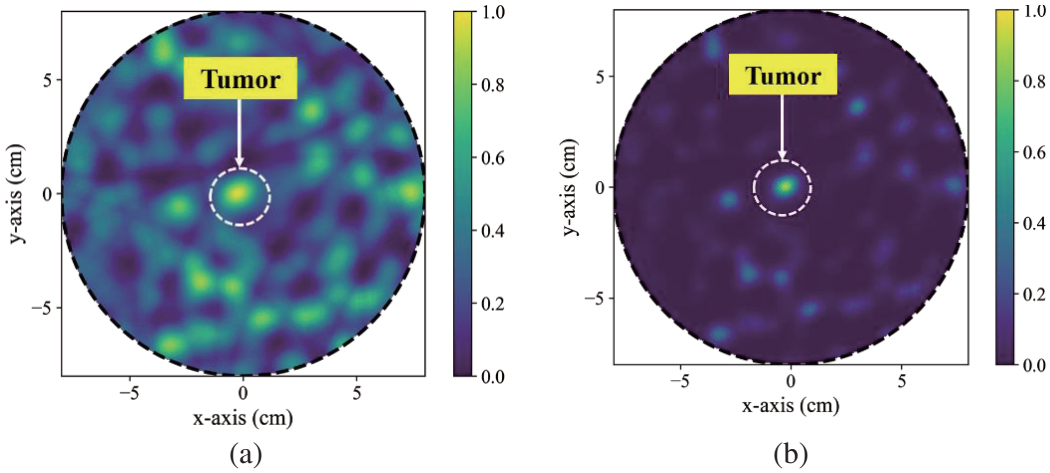

Figure 16. The reconstructed images of the homogeneous breast phantom using (a) DAS and (b) it-DAS process.

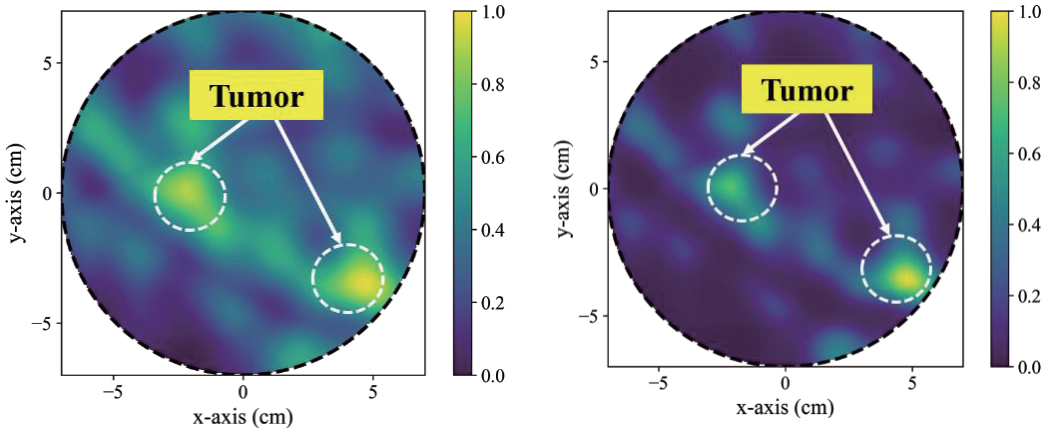

(a) (b)

Figure 17. The reconstructed images of the heterogeneous breast phantom using (a) DAS and (b) it-DAS process.

5. CONCLUSION

An SC-AVA operating in the range of 1.1–10 GHz, having a peak gain of 10.3 dBi is introduced in the proposed work for MI applications. A homogeneous breast phantom and a heterogeneous breast phantom are modelled in this work followed by fabricating the same in the lab. SAR analysis of the SC-AVA with the modelled breast phantom is done first. This is followed by using the antenna to reconstruct the tumors embedded inside the modelled breast phantoms. The single tumor embedded inside the homogeneous breast phantom and the two tumors embedded inside the heterogeneous breast phantom are reconstructed clearly in this work. The antenna along with the multiple algorithms will be used to image the same phantoms in a multistatic arrangement to obtain better quality images of the target. The developed SC-AVA will be further utilized for nondestructive testing of various concealed metallic and non-metallic targets.

ACKNOWLEDGMENT

One of the authors would like to thank the IEEE Antenna and Propagation Society (AP- S) for awarding the APS Fellowship grant — Doctoral level in 2022. Authors are grateful to the Science and Engineering Research Board, Government of India under project no: TTR/2022/000001 for funding. Authors are also grateful to the Exploratory Research Grant, Indian Institute of Technology Palakkad for partial funding.

REFERENCES

1. Siegel, R., K. Miller, H. Fuchs, and A. Jemal, "Cancer statistics," *CA Cancer J. Clin.*, Vol. 72, 7–33, 2022.
2. Bray, F., J. Ferlay, I. Soerjomataram, R. L. Siegel, L. A. Torre, and A. Jemal, "Global cancer statistics 2018: GLOBOCAN estimates of incidence and mortality worldwide for 36 cancers in 185 countries," *CA Cancer J. Clin.*, Vol. 68, 394–424, 2018.
3. Molaei A., A. Bisulco, L. Tirado, et al., "3-D-printed E-band compressive horn antenna for high-sensing-capacity imaging applications," *IEEE Antennas and Wireless Propagation Letters*, Vol. 17, No. 9, 1639–1642, Sept. 2018, doi: 10.1109/LAWP.2018.2859912.
4. Abbak, M., M. N. Akinci, M. Çayören, and I. Akduman, "Experimental microwave imaging with a novel corrugated Vivaldi antenna," *IEEE Trans. Antennas Propag.*, Vol. 65, No. 6, 3302–3307, Jun. 2017.

5. Salvador, S. M., E. C. Fear, M. Okoniewski, and J. R. Matyas, "Exploring joint tissues with microwave imaging," *IEEE Trans. Microw. Theory Techn.*, Vol. 58, No. 8, 2307–2313, Aug. 2010.
6. Islam, M., M. Samsuzzaman, M. Islam, S. Kibria, and M. Singh, "A homogeneous breast phantom measurement system with an improved modified microwave imaging antenna sensor," *Sensors*, Vol. 18, No. 9, 2962, 2018.
7. Porter, E., H. Bahrami, A. Santorelli, B. Gosselin, L. A. Rusch, and M. Popović, "A wearable microwave antenna array for time-domain breast tumor screening," *IEEE Trans. Med. Imag.*, Vol. 35, No. 6, 1501–1509, Jun. 2016.
8. Islam, M. M., M. T. Islam, M. R. I. Faruque, M. Samsuzzaman, N. Misran, and H. Arshad, "Microwave imaging sensor using compact metamaterial UWB antenna with a high correlation factor," *Materials*, Vol. 8, No. 8, 4631–4651, 2015.
9. Moosazadeh, M., "High-gain antipodal vivaldi antenna surrounded by dielectric for wideband applications," *IEEE Trans. Antennas Propag.*, Vol. 66, No. 8, 4349–4352, Aug. 2018.
10. Yesilyurt, O. and G. Turhan-Sayan, "Metasurface lens for ultra-wideband planar antenna," *IEEE Trans. Antennas Propag.*, Vol. 68, No. 2, 719–726, Feb. 2020.
11. Sang, L., S. Wu, G. Liu, J. Wang, and W. Huang, "High-gain UWB Vivaldi antenna loaded with reconfigurable 3-D phase adjusting unit lens," *IEEE Antennas Wireless Propag. Lett.*, Vol. 19, No. 2, 322–326, Feb. 2020.
12. Shi, X., Y. Lu, J. Shi, Y. Xiong, and X. Lou, "High-gain Vivaldi antipodal broadband antenna with a CSRR array and T-shaped strips," *Proc. 9th Asia-Pacific Conf. Antennas Propag.*, 1–2, Xiamen, China, 2020.
13. Shi, X., Y. Cao, Y. Hu, X. Luo, H. Yang, and L. H. Ye, "A high-gain antipodal vivaldi antenna with director and metamaterial at 1–28 GHz," *IEEE Antennas Wireless Propag. Lett.*, Vol. 20, No. 12, 2432–2436, Dec. 2021, doi: 10.1109/LAWP.2021.3114061.
14. Asok, A. O., A. N. Jaleel, and S. Dey, "Microwave imaging over UWB with antipodal Vivaldi antenna for concealed weapon detection," *2020 IEEE MTT-S Latin America Microwave Conference (LAMC 2020)*, 1–4, 2021, doi: 10.1109/LAMC50424.2021.9602491.
15. Talukder, M., M. Samsuzzaman, M. Islam, R. Azim, M. Mahmud, and M. Islam, "Compact ellipse shaped patch with ground slotted broadband monopole patch antenna for head imaging applications," *Chinese Journal of Physics*, Vol. 72, No. 5, 310–326, 2021.
16. Islam, M. T., M. Samsuzzaman, S. Kibria, and M. T. Islam, "Experimental breast phantoms for estimation of breast tumor using microwave imaging systems," *IEEE Access*, Vol. 6, 78587–78597, 2018, doi: 10.1109/ACCESS.2018.2885087.
17. Shepp, L. A. and Y. Vardi, "Maximum likelihood reconstruction for emission tomography," *IEEE Trans. Med. Imag.*, Vol. 1, No. 2, 113–122, Oct. 1982.
18. Lim, H. B., N. T. Nhung, E. P. Li, and N. D. Thang, "Confocal microwave imaging for breast cancer detection: Delay-multiply-and-Sum image reconstruction algorithm," *IEEE Trans. Biomed. Eng.*, Vol. 55, No. 6, 1697–1704, Jun. 2008.
19. Islam, M. T., M. Samsuzzaman, S. Kibria, N. Misran, and M. T. Islam, "Metasurface loaded high gain antenna based microwave imaging using iteratively corrected delay multiply and sum algorithm," *Sci. Rep.*, Vol. 9, No. 1, 1–14, Dec. 2019.
20. Islam, M. T., M. Z. Mahmud, M. T. Islam, S. Kibria, and M. Samsuzzaman, "A low cost and portable microwave imaging system for breast tumor detection using UWB directional antenna array," *Sci. Rep.*, Vol. 9, No. 1, 1–13, Dec. 2019.
21. Islam, M., M. Samsuzzaman, M. Islam, S. Kibria, and M. Singh, "A homogeneous breast phantom measurement system with an improved modified microwave imaging antenna sensor," *Sensors*, Vol. 18, No. 9, 2962, 2018.
22. Shao, W., A. Edalati, T. R. McCollough, and W. J. McCollough, "A time-domain measurement system for UWB microwave imaging," *IEEE Trans. Microw. Theory Techn*, Vol. 66, No. 5, 2265–2275, 2018.

23. Mahmud, M. Z., M. T. Islam, N. Misran, S. Kibria, and M. Samsuzzaman, "Microwave imaging for breast tumor detection using uniplanar AMC based CPW-fed microstrip antenna," *IEEE Access*, Vol. 6, 44763–44775, 2018, doi: 10.1109/ACCESS.2018.2859434.
24. Porter, E., H. Bahrami, A. Santorelli, et al., "A wearable microwave antenna array for time-domain breast tumor screening," *IEEE Trans. Med. Imag.*, Vol. 35, No. 6, 1501–1509, Jun. 2016.
25. Zerrad, F.-E., M. Taouzari, E. M. Makroum, J. El Aoufi, M. T. Islam, V. Özkaner, Y. I. Abdulkarim, and M. Karaaslan, "Multilayered meta-materials array antenna based on artificial magnetic conductor's structure for the application diagnostic breast cancer detection with microwave imaging," *Med. Eng. Phys.*, Vol. 99, Art. No. 103737, Jan. 2022, doi: 10.1016/j.medengphy.2021.103737.
26. Bhargava, D. and P. Rattanadecho, "Microstrip antenna for radar-based microwave imaging of breast cancer: Simulation analysis," *Int. J. Commun. Antenna Propag*, Vol. 12, 47–53, 2022.
27. Kaur, G. and A. Kaur, "Monostatic radar-based microwave imaging of breast tumor using an ultra-wideband dielectric resonator antenna (DRA) with a Sierpinski fractal defected ground structure," *MAPAN*, Vol. 37, No. 4, 917–928, 2022.
28. Syed, A., M. Sheikh, M. T. Islam, and H. Rmili, "Metamaterial-loaded 16-printed log periodic antenna array for microwave imaging of breast tumor detection," *Int. J. Antennas Propag.*, 2022.
29. Dey, A. B. and W. Arif, "Design and analysis of a CPW-fed flexible ultrawideband antenna for microwave imaging of breast cancer," *Int. J. RF Microw. Comput. Aided Eng.*, Vol. 32, No. 9, e23262, 2022.
30. Abbak, M., M. Çayören, and I. Akduman, "Microwave breast phantom measurements with a cavity-backed Vivaldi antenna," *IET Microw., Antennas Propag.*, Vol. 8, No. 13, 1127–1133, Oct. 2014.
31. Wu, B., Y. Ji, and G. Fang, "Design and measurement of compact tapered slot antenna for UWB microwave imaging radar," *Proc. 9th Int. Conf. Electron. Meas. Instrum. (ICEMI)*, 2-226–2-229, 2009.
32. Islam, M. T., M. Z. Mahmud, N. Misran, J.-I. Takada, and M. Cho, "Microwave breast phantom measurement system with compact side slotted directional antenna," *IEEE Access*, Vol. 5, 5321–5330, 2017.
33. Samsuzzaman, M., M. T. Islam, M. T. Islam, A. A. S. Shovon, R. I. Faruque, and N. Misran, "A 16-modified antipodal Vivaldi antenna array for microwave-based breast tumor imaging applications," *Microw. Opt. Technol. Lett.*, Vol. 61, 2110–2118, 2019, https://doi.org/10.1002/mop.31873.
34. Porter, E., E. Kirshin, A. Santorelli, M. Coates, and M. Popović, "Time-domain multistatic radar system for microwave breast screening," *IEEE Antennas Wireless Propag. Lett.*, Vol. 12, 229–232, 2013.
35. Porter, E., H. Bahrami, A. Santorelli, B. Gosselin, L. A. Rusch, and M. Popović, "A wearable microwave antenna array for time-domain breast tumor screening," *IEEE Trans. Med. Imag.*, Vol. 35, No. 6, 1501–1509, Jun. 2016.
36. Sugitani, T., S. Kubota, A. Toya, X. Xiao, and T. Kikkawa, "A compact 4×4 planar UWB antenna array for 3-D breast cancer detection," *IEEE Antennas Wireless Propag. Lett.*, Vol. 12, 733–736, 2013.
37. Islam, M. T., M. Samsuzzaman, M. Faruque, M. J. Singh, and M. Islam, "Microwave imaging based breast tumor detection using compact wide slotted UWB patch antenna," *Optoelectron. Adv. Mater. Rapid Commun.*, Vol. 13, 448–457, 2019.
38. Bhattacharjee, A., A. Bhawal, A. Karmakar, A. Saha, and D. Bhattacharya, "Vivaldi antennas: A historical review and current state of art," *International Journal of Microwave and Wireless Technologies*, Vol. 13, No. 8, 833–850, 2021, doi:10.1017/S1759078720001415.
39. Asok, A. O., G. Nath, and S. Dey, "Microwave imaging with novel time-domain clutter removal algorithm using high gain antennas for concealed object detections," *IEEE Transactions on Computational Imaging*, Vol. 9, 147–158, 2023, doi: 10.1109/TCI.2023.3244392.
40. Asok, A. O., S. J. G. Nath, and S. Dey, "Concealed object detection with microwave imaging using vivaldi antennas utilizing novel time-domain beamforming algorithm," *IEEE Access*, Vol. 10, 116987–117000, 2022, doi: 10.1109/ACCESS.2022.3218892.

41. Asok, A. O., S. J. G. Nath, and S. Dey, "Non-invasive breast tumor detection with antipodal Vivaldi antenna using monostatic approach," *Int. J. RF Microw. Comput. Aided Eng.*, e23539, 2022, doi:10.1002/mmce.2353914 of 14ASOKET AL.
42. Asok, A. O., R. Anjaly, S. Dey, and N. Kunju, "Monopole antenna loaded with wind mill shaped FSS for breast tumor detection," *2023 First International Conference on Microwave, Antenna and Communication (MAC)*, 1–4, Prayagraj, India, 2023, doi: 10.1109/MAC58191.2023.10177126.
43. Asok, A. O., N. Kunju, and S. Dey, "Microwave medical imaging using a compact monopole antenna for brain tumor detection," *2023 First International Conference on Microwave, Antenna and Communication (MAC)*, 1–4, Prayagraj, India, 2023, doi: 10.1109/MAC58191.2023.10177071.
44. Asok, A. O., M. A. Shukoor, and S. Dey, "Breast cancer detection with metamerial enabled monopole antennas using microwave imaging," *2022 IEEE International Conference on Emerging Electronics (ICEE)*, 1–4, Bangalore, India, 2022, doi: 10.1109/ICEE56203.2022.10118050.
45. Asok, A. O., S. J. Gokul Nath, S. J. Vidhya, N. Kunju, and S. Dey, "Brain tumor detection with compact monopole antennas using microwave medical imaging," *2022 IEEE Microwaves, Antennas, and Propagation Conference (MAPCON)*, 439–443, Bangalore, India, 2022, doi: 10.1109/MAPCON56011.2022.10047439.
46. Asok, A. O., J. S. Vidhya, N. Kunju, and S. Dey, "Wearable, conformal, compact and flexible F-slot monopole antenna on textile for non-invasive biomedical imaging," *2022 IEEE Microwaves, Antennas, and Propagation Conference (MAPCON)*, 465–470, Bangalore, India, 2022, doi: 10.1109/MAPCON56011.2022.10047333.
47. Asok, A. O., J. S. Vidhya, F. Bethel Babu, S. Dey, and N. Kunju, "Metamerial-based monopole antenna for breast cancer detection," *2022 IEEE 19th India Council International Conference (INDICON)*, 1–4, Kochi, India, 2022, doi: 10.1109/INDICON56171.2022.10039765.
48. Asok, A. O., G. N. S. J, A. Tripathi, S. Chauhan, K. S. Kiran, and S. Dey, "Double ridge conical horn antenna with dielectric loading for microwave imaging of human breast," *2022 IEEE Wireless Antenna and Microwave Symposium (WAMS)*, 1–4, Rourkela, India, 2022, doi: 10.1109/WAMS54719.2022.9848224.
49. Nath, G. S. J., A. O. Asok, and S. Dey, "Metallic object detection inside human stomach with antipodal Vivaldi antenna utilizing microwave imaging technique," *2022 IEEE Wireless Antenna and Microwave Symposium (WAMS)*, 1–4, Rourkela, India, 2022, doi: 10.1109/WAMS54719.2022.9848254.
50. Asok, A. O., S. J. G. Nath, and S. Dey, "Double ridge horn antenna with curved dielectric loading for microwave imaging applications," *2021 IEEE Indian Conference on Antennas and Propagation (InCAP)*, 167–170, Jaipur, Rajasthan, India, 2021, doi: 10.1109/InCAP52216.2021.9726351.
51. Asok, A. O. and S. Dey, "UWB antipodal antenna with parasitic patch and elliptical cylindrical dielectric for concealed object detection with microwave imaging," *2021 IEEE International Symposium on Antennas and Propagation and USNC-URSI Radio Science Meeting (APS/URSI)*, 741–742, Singapore, 2021, doi: 10.1109/APS/URSI47566.2021.9704371.
52. Asok, A. O. and S. Dey, "UWB antipodal vivaldi antenna with metamaterial slabs and dielectric enclosure for microwave to millimeter wave imaging applications," *2021 IEEE Asia-Pacific Microwave Conference (APMC)*, 49–51, Brisbane, Australia, 2021, doi: 10.1109/APMC52720.2021.9661587.
53. Asok, A. O., S. J. G. Nath, and S. Dey, "Microwave breast imaging using synthetic aperture radar method utilizing UWB antenna," *2020 IEEE MTT-S Latin America Microwave Conference (LAMC 2020)*, 1–4, Cali, Colombia, 2021, doi: 10.1109/LAMC50424.2021.9601445.
54. Asok, A. O. and S. Dey, "Novel UWB antipodal antenna with paddle shaped stubs and frustum shaped dielectric loading for microwave imaging applications," *2020 IEEE Asia-Pacific Microwave Conference (APMC)*, 1060–1062, Hong Kong, Hong Kong, 2020, doi: 10.1109/APMC47863.2020.9331467.
55. Reimer, T., M. Solis-Nepote, and S. Pistorius, "The application of an iterative structure to the delay-and-sum and the delay-multiply-and-sum beamformers in breast microwave imaging," *Diagnostics*, Vol. 10, No. 6, 411–426, 2020.

56. Reimer, T., J. Krenkevich, and S. Pistorius, "An open-access experimental dataset for breast microwave imaging," *2020 14th European Conference on Antennas and Propagation (EuCAP)*, 1–5, Copenhagen, Denmark, 2020, doi: 10.23919/EuCAP48036.2020.9135659.